Journal of the Korean Society for Nondestructive Testing
Vol. 23, No. 6 (2003. 12)

Analytical Beam Field Modeling Applied to Transducer Optimization and Inspection Simulation in Ultrasonic Nondestructive Testing

Martin Spies

Abstract To ensure the reliability of ultrasonic nondestructive testing techniques for modern structural materials, the effects of anisotropy and inhomogeneity and the influence of non-planar component geometries on ultrasonic wave propagation have to be taken into account. In this article, fundamentals and applications of two analytical approaches to three-dimensional elastic beam field calculation are presented. Results for both isotropic materials including curved interfaces and for anisotropic media like composites are presented, covering field profiles for various types of transducers and the modeling of time-dependent rf-signals.

Keywords: modeling, ultrasonics, transducer, anisotropy, inspection

1. Introduction

In ultrasonic nondestructive evaluation use is made of the physical properties of elastic waves in solids in order to detect defects and material inhomogeneities. To ensure the reliability of ultrasonic inspection techniques for modern structural materials, the effects of anisotropy and inhomogeneity and the effects of non-planar component geometries on ultrasonic wave propagation have to be taken into account. In this article, fundamentals and applications of two analytical approaches to three-dimensional elastic wavefield calculation are presented, which can applied to model ultrasound generation, propagation and scattering in complex-structured materials and components.

Based on a mathematical formulation involving Green's dyadic displacement tensor function, appropriate evaluation yields a representation of the displacement vector of transducer wavefields which is convenient for effective numerical computation. With respect to bulk wave propagation the numerical evaluation of Green's dyadic function - which is particularly tedious in the anisotropic case - is circumvented by applying a reciprocity-based approach. The presented formulation involves characteristic quantities obtained from plane wave theory and appears as a point source superposition representation including the respective point source directivities. The approach allows to include all aspects relevant to testing simulation for such configurations as far as bulk wave propagation is concerned (Spies, 1994a; Spies, 2001). The results obtained using this approach are valid even in the near-field of the beam. Based on the presented formulation, efficient far-field approximations have been derived in (Spies, 2002a), which is particularly useful in view of low calculation times. This will also be addressed in this article.

Representative results for both isotropic materials including curved interfaces and for anisotropic media like composites are presented, covering field

Received: September 17, 2003. Accepted: November 14, 2003. * Fraunhofer-Institut Zerstörungsfreie Rrüfverfahren (IZFP), Universität, Geb. 37, 66123 Saarbrücken, Germany

profiles for various types of transducers and the modeling of time-dependent rf-signals. Simulation-assisted transducer optimization is also illustrated for both single-element and multiple-element probes.

2. Fundamentals

2.1. Equation of Motion

The dynamic behaviour of a linear elastic medium can be described by the equation of motion for the displacement vector $\underline{\mathbf{u}}$. For a homogeneous solid it can be written in a general form according to

$$(\underline{\nabla} \cdot \underline{\underline{\underline{\mathbf{C}}}} \cdot \underline{\nabla}) \cdot \underline{\mathbf{u}} + \varrho\omega^2 \underline{\mathbf{u}} = -\,\underline{\mathbf{f}}\,, \tag{1}$$

where ϱ is the mass density, $\underline{\nabla}$ is the gradient vector, $\underline{\mathbf{f}}$ accounts for the volume force density and ω denotes the circular frequency, if a time dependence $\sim \mathrm{e}^{-\mathrm{j}\omega t}$ is assumed. The elastic properties of the homogeneous solid are described by the fourth rank elastic (stiffness) tensor, which depends on the elastic material constants. A most general representation for this tensor has been given recently for orthotropic media of arbitrary orientation (Spies, 2001), which includes the higher symmetries tetragonal, transversely isotropic, cubic and isotropic as special cases.

2.2. Plane Waves

The plane wave solutions are in the form

$$\underline{\mathbf{u}}_\alpha(\underline{\mathbf{R}}, \omega) = U\, \underline{\hat{\mathbf{u}}}_\alpha \exp\left[\mathrm{j}\, K_\alpha \underline{\hat{\mathbf{K}}} \cdot \underline{\mathbf{R}}\right], \tag{2}$$

where $\underline{\hat{\mathbf{K}}}$ is the propagation direction, U is the (complex) amplitude and α denotes the wave type. The determination of the polarization vectors $\underline{\hat{\mathbf{u}}}_\alpha$ and the wave numbers K_α can be performed by applying Fourier-transforms with respect to $\underline{\mathbf{R}}$ in terms of

$$\underline{\tilde{\mathbf{u}}}(\underline{\mathbf{K}}, \omega) = \int_{-\infty}^{\infty} \underline{\mathbf{u}}(\underline{\mathbf{R}}, \omega)\, \mathrm{e}^{-\mathrm{j}\underline{\mathbf{K}}\cdot\underline{\mathbf{R}}}\, \mathrm{d}^3\underline{\mathbf{R}} \tag{3}$$

to the equation of motion (1) for $\underline{\mathbf{f}} = \underline{\mathbf{0}}$. This yields the dispersion equation

$$\underline{\underline{\tilde{\mathbf{W}}}}(\underline{\mathbf{K}}, \omega) \cdot \underline{\tilde{\mathbf{u}}}(\underline{\mathbf{K}}, \omega) = \underline{\mathbf{0}}\,, \tag{4}$$

where the tilde denotes the transformed quantities. In this equation, the 3d-space-time-Fourier representation of $\underline{\mathbf{u}}$ appears as well as the wave matrix

$$\underline{\underline{\tilde{\mathbf{W}}}}(\underline{\mathbf{K}}, \omega) = \underline{\mathbf{K}} \cdot \underline{\underline{\underline{\mathbf{C}}}} \cdot \underline{\mathbf{K}} - \varrho\omega^2\, \underline{\underline{\mathbf{I}}}\,, \tag{5}$$

where $\underline{\underline{\mathbf{I}}}$ is the unity matrix. The polarization vectors $\underline{\hat{\mathbf{u}}}_\alpha$ and the wave numbers K_α can be obtained as the eigenvectors and the eigenvalues of the wave matrix. The latter provide the modulus of phase velocity v_α according to $v_\alpha = |\, \underline{\mathbf{s}}_\alpha \,|^{-1}$ with slowness $\underline{\mathbf{s}}_\alpha = K_\alpha \underline{\hat{\mathbf{K}}} \,/\omega$.

In anisotropic media, the phase velocity is different from the velocity of energy transport, which is in the case of lossless materials given by the group velocity according to

$$\underline{\mathbf{c}}_\alpha = \left(v\, \frac{\partial K}{\partial \underline{\mathbf{K}}} + K\, \frac{\partial v}{\partial \underline{\mathbf{K}}}\right)_{\underline{\mathbf{K}}_\alpha} \tag{6}$$

For transversely isotropic and orthotropic materials with arbitrary spatial orientation, these quantities have been given previously (Spies, 1994a; Spies, 2001).

2.3. Bulk Wave Properties

In an isotropic medium, one can distinguish between the compressional (P) and the horizontally or vertically polarized shear waves (SH and SV). The decomposition into these three eigenwaves is based on the orientation of the polarization vectors with respect to the horizontal plane. In a weakly anisotropic medium, the plane waves can still be labeled as quasi-P (qP), with approximately longitudinal polarization, and quasi-SH (qSH) and quasi-SV (qSV), with approximately transverse polarization. In a strongly anisotropic medium, there are three plane waves with mutually orthogonal polarizations in every direction of propagation. These are designated as qP, $qS1$ and $qS2$ according to their polarizations when propagated in certain symmetry directions. The speeds of these waves are different and vary with direction. Additionally, the directions of phase flow and energy flow involved with these waves are different, so that phase and group velocity have to be discerned.

2.4. Consideration of Multilayered Media

Each interface between the layers produces reflected and refracted waves, which is considered by evaluating the respective conditions of continuity. For planar interfaces, Cartesian coordinates with unit vectors $\{\underline{\mathbf{e}}_x, \underline{\mathbf{e}}_y, \underline{\mathbf{e}}_z\}$ can be used, so that the interface lies in the x-y-plane. Assuming ideal rigid contact between adjacent layers requires the continuity of the slownesses ($\underline{\mathbf{s}} \cdot \underline{\mathbf{e}}_i$ continuous, $i = x, y$, 'Snell's law') and the continuity of the particle displacements and the normal tractions according to

$$U^I \underline{\mathbf{u}}^I + \sum_\alpha U^{R\alpha} \underline{\mathbf{u}}^{R\alpha} = \sum_\alpha U^{T\alpha} \underline{\mathbf{u}}^{T\alpha}, \quad (7)$$

$$\underline{\mathbf{e}}_z \cdot \underline{\underline{\mathbf{T}}}^I + \sum_\alpha \underline{\mathbf{e}}_z \cdot \underline{\underline{\mathbf{T}}}^{R\alpha} = \sum_\alpha \underline{\mathbf{e}}_z \cdot \underline{\underline{\mathbf{T}}}^{T\alpha}, \quad (8)$$

where $\underline{\underline{\mathbf{T}}}$ designates the stress tensor. From these equations, the amplitudes $U^{R\alpha}$ and $U^{T\alpha}$ of the reflected and transmitted waves of type α can be determined in dependence of the incident amplitude U^I. In the case of non-planar interfaces, these boundary conditions have to be applied locally. The local structure of an inhomogeneous medium can be described by dividing it into several layers, each of them having different elastic properties, as has been described for layered transversely isotropic media in (Spies, 1994b).

3. Analytical Modeling Approaches

3.1. Point Source Superposition

The basis for the elastodynamic beam field calculation procedure presented here is the mathematical formulation of Huygens' principle (Pao and Varatharajulu, 1976). For wave radiation by an isolated vibrating body or a fixed surface enclosing a source, where each point on the surface S of the body vibrates with the same angular frequency ω, the displacement vector outside the surface S can be written as

$$\underline{\mathbf{u}}(\underline{\mathbf{R}}, \omega) = \int\int_S \Big\{ \underline{\mathbf{u}}(\underline{\mathbf{R}}', \omega) \cdot \Big[\underline{\mathbf{n}} \cdot \underline{\underline{\mathbf{\Sigma}}}(\Delta\underline{\mathbf{R}}, \omega) \Big] - \Big[\underline{\mathbf{n}} \cdot \underline{\underline{\mathbf{T}}}(\underline{\mathbf{R}}', \omega) \Big] \cdot \underline{\underline{\mathbf{G}}}(\Delta\underline{\mathbf{R}}, \omega) \Big\} \, \mathrm{d}S', \quad (9)$$

where - with $\underline{\underline{\mathbf{T}}}$ being the stress tensor - the traction $\underline{\mathbf{n}} \cdot \underline{\underline{\mathbf{T}}}$ and the displacement $\underline{\mathbf{u}}$ at this surface act as sources of the generated wavefield. With $\Delta\underline{\mathbf{R}} \equiv (\underline{\mathbf{R}} - \underline{\mathbf{R}}')$, $\underline{\underline{\mathbf{G}}}$ and $\underline{\underline{\underline{\mathbf{\Sigma}}}}$ are Green's dyadic and triadic functions, whose components represent the displacement and stress field, respectively, at position $\underline{\mathbf{R}}$ generated by three mutually perpendicular (point) forces acting at $\underline{\mathbf{R}}'$ on surface S.

For evaluating transducer radiation, S is assumed to lie in the x-y-plane of a Cartesian coordinate system, i.e. $\underline{\mathbf{n}} = \underline{\mathbf{e}}_z$. In selecting the Green's tensor functions entering in Eq. (9) one has two options. The first one is to choose the free-space functions as has been done e.g. in (Guo and Achenbach, 1995), where, however, $\underline{\mathbf{u}}(\underline{\mathbf{R}}', \omega)$ is an unknown function which has to be determined. Here, the Green's functions for the elastic half-space are chosen, where - considering the surface to be stress-free - the triadic stress-tensor function accordingly fulfills the boundary condition that

$$\underline{\mathbf{e}}_z \cdot \underline{\underline{\underline{\mathbf{\Sigma}}}}^{half} \Big|_{z=0} = \underline{\underline{\mathbf{0}}}, \quad (10)$$

so that

$$\underline{\mathbf{u}}(\underline{\mathbf{R}}, \omega) = -\iint_S \Big[\underline{\mathbf{e}}_z \cdot \underline{\underline{\mathbf{T}}}(\underline{\mathbf{R}}', \omega) \Big] \cdot \underline{\underline{\mathbf{G}}}^{half}(\Delta\underline{\mathbf{R}}, \omega) \mathrm{d}S' \quad (11)$$

follows, where the dyadic Green's function for the half-space has accordingly been introduced.

From (Wu et al., 1991), where the far-field radiation of vibrating point sources in anisotropic media is considered, a far-field expression for $\underline{\underline{\mathbf{G}}}^{half}$ accounting for the bulk wave contributions can be inferred according to

$$\underline{\underline{\mathbf{G}}}^{half}_{far}(\Delta\underline{\mathbf{R}}, \omega) = \sum_\alpha \underline{\mathbf{g}}_\alpha \Big(\underline{\hat{\mathbf{K}}}(\widehat{\Delta\underline{\mathbf{R}}}) \Big) \, \underline{\hat{\mathbf{u}}}_\alpha \Big(\underline{\hat{\mathbf{K}}}(\widehat{\Delta\underline{\mathbf{R}}}) \Big) \times \frac{e^{j\underline{\mathbf{K}}_\alpha(\widehat{\Delta\underline{\mathbf{R}}}) \cdot \Delta\underline{\mathbf{R}}}}{4\pi \mid \Delta\underline{\mathbf{R}} \mid}, \quad (12)$$

where $\underline{\hat{\mathbf{u}}}_\alpha$ and $\underline{\mathbf{K}}_\alpha = K_\alpha \underline{\hat{\mathbf{K}}}$ designate the (plane wave) polarization vector and the wave vector of wavetype α, respectively. The Cartesian components of vector $\underline{\mathbf{g}}_\alpha$ are the directivities for transversely (in x- or y-direction) and normally (in z-direction) acting point sources on the stress-free surface. $\underline{\mathbf{g}}_\alpha$ and $\underline{\hat{\mathbf{u}}}_\alpha$ - as well as the group velocity vector $\underline{\mathbf{c}}_\alpha$ - are functions of the wave propagation direction $\underline{\hat{\mathbf{K}}}$ that produces an energy contribution along the spatial direction $\widehat{\Delta\underline{\mathbf{R}}}$. An efficient numerical evaluation scheme for the $\underline{\hat{\mathbf{K}}}(\widehat{\Delta\underline{\mathbf{R}}})$-relationship has been described in

(Spies, 2001). In directions where group velocity is multivalued the different wave decay properties ($\mathcal{O}(R^{-1/2})$ and $\mathcal{O}(R^{-5/6})$ instead of $\mathcal{O}(R^{-1})$) have to be taken into account, as described in (Spies, 2002b). Using Eq. (12) and defining the surface traction

$$\underline{\mathbf{t}}(\underline{\mathbf{R}}',\omega) \equiv \underline{\mathbf{e}}_z \cdot \underline{\underline{\mathbf{T}}}(\underline{\mathbf{R}}',\omega)\ , \tag{13}$$

Eq. (11) finally leads to

$$\underline{\mathbf{u}}(\underline{\mathbf{R}},\omega) \cong -\int\!\!\int_S \sum_\alpha \left[\underline{\mathbf{t}}(\underline{\mathbf{R}}',\omega)\cdot\underline{\mathbf{g}}_\alpha\Big(\hat{\underline{\mathbf{K}}}(\widehat{\Delta\underline{\mathbf{R}}})\Big)\right] \times\hat{\underline{\mathbf{u}}}_\alpha\Big(\hat{\underline{\mathbf{K}}}(\widehat{\Delta\underline{\mathbf{R}}})\Big)\frac{e^{j\omega|\underline{\mathbf{R}}-\underline{\mathbf{R}}'|/c_\alpha(\widehat{\Delta\underline{\mathbf{R}}})}}{4\pi\mid\Delta\underline{\mathbf{R}}\mid}\,dS', \tag{14}$$

which is valid in the far-field of the point source, and which can be applied to model transducer generated bulk wave fields in isotropic and anisotropic media. To circumvent the intricate determination of $\underline{\mathbf{g}}_\alpha$ using Green's function, a method based on the reciprocity theorem is applied (Wu et al., 1990).

Assuming a traction whose magnitude is zero outside the transducer aperture and unity within, the integration in Eq. (14) has to be performed over the transducer aperture. Numerical integration on the basis of an equally spaced rectangular grid can be applied for planar surfaces, with grid points separated at a distance of less than half a wavelength to fulfil the sampling theorem. For curved - e.g. cylindrical or spherical - surfaces a respective projection of a planar grid onto the curved surfaces is applied. If multiple element transducers are considered, the aperture is accordingly structured with tractions of zero or unity magnitude, respectively, where also additional phase delays can be introduced. The results obtained for continuous wave displacement fields using this computational scheme are valid even in the near-field of the beam (Spies, 2001). On the basis of Eq. (14), an efficient far-field approximation has been derived in (Spies, 2002a), which is summarized below.

In order to determine transducer beam fields for broadband input signals, a straight-forward computational approach for modeling of transient signals is applied, where the harmonic (cw) solution is calculated at many frequencies and then this data is numerically Fourier transformed into the time domain. In this approach, a function for the frequency spectrum of the transducer input signal has to be selected, e.g. to properly model an experimental input signal.

In modeling the insonification into a component using immersion technique, the evaluation of Eq. (14) is performed accordingly. The particle displacement is calculated at the interface grid points and used as the prescribed displacement distribution at this interface. Taking into account the respective boundary conditions, this distribution is then propagated from the interface into the material as described above. The same principle holds for defects and other discontinuities with consideration of the appropriate point source directivities. Based on Kirchhoff's theory, this has been presented previously in (Spies, 2000).

3.2. Far-Field Approximation

Neglecting the influence of the traction-free material/defect surface, characterized by the respective point source directivities, the radiation behaviour of the vibrating source with aperture S follows from Eq. (1) according to

$$|\,\underline{\mathbf{u}}_\alpha(\underline{\mathrm{R}},\omega)\,| \cong \frac{1}{4\pi}\int\!\!\int_S \frac{e^{j\underline{\mathbf{K}}_\alpha(\widehat{\underline{\mathbf{R}}-\underline{\mathbf{R}}'})\cdot(\underline{\mathbf{R}}-\underline{\mathbf{R}}')}}{|\,\underline{\mathbf{R}}-\underline{\mathbf{R}}'\,|}\,dS'. \tag{15}$$

In the far-field, where $R \gg R'$, it is

$$|\underline{\mathbf{R}}-\underline{\mathbf{R}}'| \cong R - \hat{\underline{\mathbf{R}}}\cdot\underline{\mathbf{R}}'\ , \tag{16}$$

$$\underline{\mathbf{K}}_\alpha(\widehat{\underline{\mathbf{R}}-\underline{\mathbf{R}}'}) \cong \underline{\mathbf{K}}_\alpha(\hat{\underline{\mathbf{R}}})\ , \tag{17}$$

and thus

$$|\,\underline{\mathbf{u}}_\alpha^{far}(\underline{\mathrm{R}},\omega)\,| = \frac{1}{4\pi R}\exp\Big(j\underline{\mathbf{K}}_\alpha(\hat{\underline{\mathbf{R}}})\cdot\underline{\mathbf{R}}\Big) \times\int\!\!\int_S \exp\Big(-j\underline{\mathbf{K}}_\alpha(\hat{\underline{\mathbf{R}}})\cdot\underline{\mathbf{R}}'\Big)dS'. \tag{18}$$

The integral in this equation can be solved as in the isotropic case (Stenzel and Brosze, 1958) yielding

$$|\,\underline{\mathbf{u}}_\alpha^{far}(\underline{\mathrm{R}},\omega)\,| = A\,\frac{\exp\Big(j\omega R/c_\alpha(\hat{\underline{\mathbf{K}}}(\hat{\underline{\mathbf{R}}}))\Big)}{4\pi R}\cdot\Gamma(\hat{\underline{\mathbf{R}}}), \tag{19}$$

where the relationships $\underline{\mathbf{K}}_\alpha\cdot\underline{\mathbf{c}}_\alpha = \omega$ and $\underline{\mathbf{K}}_\alpha\cdot\underline{\mathbf{R}} = \underline{\mathbf{K}}_\alpha\cdot\underline{\mathbf{c}}_\alpha R/c_\alpha = \omega R/c_\alpha$ have been exploited, c_α being the modulus of the group velocity vector. For a circular piston source with radius a - introducing $\hat{K}_r(\hat{\underline{\mathbf{R}}}) = \sqrt{\hat{K}_x^2(\hat{\underline{\mathbf{R}}}) + \hat{K}_y^2(\hat{\underline{\mathbf{R}}})}$ - the directivity function results as

$$\Gamma_{circ}(\hat{\underline{\mathbf{R}}}) = \frac{J_1\Big(aK_\alpha(\hat{\underline{\mathbf{R}}})\hat{K}_r(\hat{\underline{\mathbf{R}}})\Big)}{\Big(aK_\alpha(\hat{\underline{\mathbf{R}}})\hat{K}_r(\hat{\underline{\mathbf{R}}})\Big)},\quad A_{circ} = 2\pi a^2, \tag{20}$$

while for a rectangular piston source of area $2a \times 2b$ it is

$$\Gamma_{rect}(\hat{\underline{\mathbf{R}}}) = \frac{\sin\left(aK_\alpha(\hat{\underline{\mathbf{R}}})\hat{K}_x(\hat{\underline{\mathbf{R}}})\right)}{\left(aK_\alpha(\hat{\underline{\mathbf{R}}})\hat{K}_x(\hat{\underline{\mathbf{R}}})\right)} \cdot \frac{\sin\left(bK_\alpha(\hat{\underline{\mathbf{R}}})\hat{K}_y(\hat{\underline{\mathbf{R}}})\right)}{\left(bK_\alpha(\hat{\underline{\mathbf{R}}})\hat{K}_y(\hat{\underline{\mathbf{R}}})\right)},$$
$$A_{rect} = 4ab. \qquad (21)$$

These expressions are the same as in the isotropic case, but here the wave numbers and the components of the $\underline{\mathbf{K}}$-vectors depend on the spatial coordinates.

4. Application to Transducer Optimization

For industrial components of arbitrary shape, the transducer fields strongly depend on the material or interface curvatures and the coupling conditions. Thus, simulation of transducer sound fields is most useful for evaluating measured signals and for designing transducers which are optimized for the respective set-up. Due to the large number of transducer parameters and their complex influence on the sound field, experimental work can thus be significantly reduced, which is useful for both single-element and multiple element transducers.

4.1. Immersion Probe for Cylindrical Component Inspection

The component to be inspected is a steel pipe with an inner diameter of 34 mm and a wall thickness of 20 mm. Using immersion technique, the pipe is assumed to be tested for defects from the interior, with high sensitivity in a range from 4 mm to 8 mm depth. Usually, the inspection of such components is performed using so called bi-focal transducers. Such line-focusing probes exhibit beam fields which are focused in the axial plane, but diverging in the radial plane, with an additional focal spot being generated due to the component's curvature. To improve the inspection performance, a transducer has been elaborated, which - operated at 10 MHz frequency - three-dimensionally focusses the beam field to a depth of 6 mm. In the optimization, both frequency and the piezoelement dimensions have been varied, while a fixed immersion distance of 15 mm has been assumed according to the inner pipe diameter. Details on the optimization procedure can be found in (Spies, submitted).

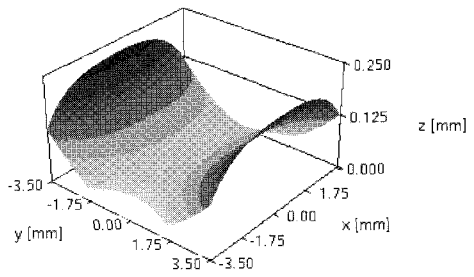

Fig. 1 Geometry of the optimized piezoelement applied to focus to a depth of 6 mm (expanded scale along z-axis)

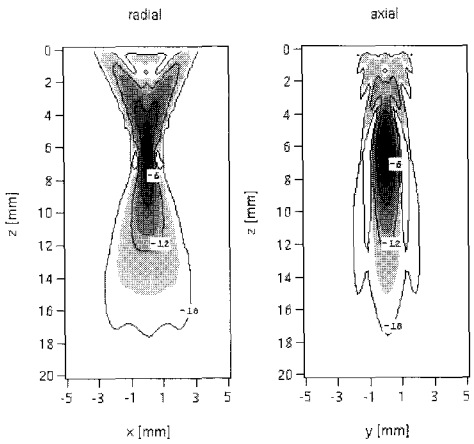

Fig. 2 Beam field representations for the optimized transducer in the radial (left) and axial (right) plane (frequency 10 MHz, immersion distance 15 mm)

As shown in Fig. 1, the calculated shape of the rectangular piezoelement of 7 x 7 mm^2 is characterized by a convex curvature of 80 mm radius in the radial plane, and a concave curvature in the axial plane (radius 40 mm). The beam field calculated for this transducer configuration is shown in Fig. 2. The desired coverage of the depth range from 4 mm to 8 mm is achieved within an amplitude range between 0 dB and -6 dB as indicated. The amplitude continuously decreases, at a depth of 15 mm it is still approximately -15 dB with respect to the absolute maximum value. For the optimized probe, the absolute maximum of the beam field is approximately 5 times as high as compared to the absolute maximum

produced by a commercial line-focusing transducer of similar dimensions (Spies, submitted).

4.2. Phased Array on Composite Material

The anisotropic elastic behaviour of modern structural materials like composites and the resulting wave propagation characteristics lead to considerable difficulties in applying conventional ultrasonic inspection procedures. However, the effects of beam field skewing and distortion can be considerably compensated by proper focusing and steering of array transducer fields (Spies et al., 2002).

As an example, the beam fields generated by a conventional angle-beam array transducer have been evaluated and optimized for a layered $[0_3/90]$-composite material. The elastic characteristics of this material are described in (Hosten et al., 1987). The 2 MHz-probe - applied to generate (quasi-) longitudinal waves - consists of a rectangular transducer (16x8 mm^2) mounted on a perspex wedge. The wedge angle is 19.6° resulting in an insonification angle of 45° in ferritic steel. In calculating the delay times for the 16 elements, the directionally dependent ultrasonic velocities have been taken into consideration. As schematically shown in Fig. 3, the delay times are determined for each element in order to focus the generated beam to a focal point with coordinates (x_f, z_f) in the plane of insonification.

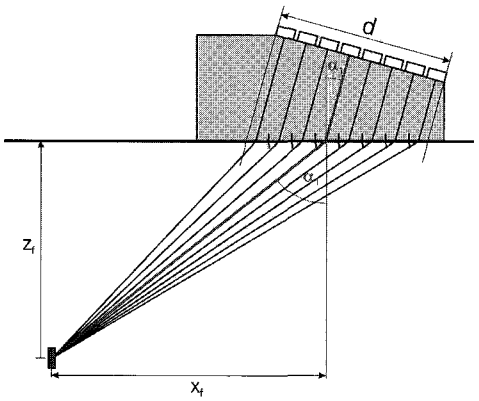

Fig. 3 Schematic sketch of a conventional angle-beam array transducer. Beam focusing to the point (x_f, z_f) is accomplished by delay time calculation using the anisotropic material's elastic properties.

Figure 4 displays polar plots of the probe's directivity patterns - calculated at a distance of $r = 40$ mm for various focal modes. The solid line represents the directivities without time-delayed excitation of the elements. As expected, the insonification angle is different from 45°, which is obtained in ferritic steel. However, point focusing allows to direct the beam field to various angles and even improve the field amplitudes, as represented by the dashed curves in Fig. 4. Thus, the difficulties usually experienced in inspecting anisotropic materials, i.e. beam skewing and distortion effects, can be considerably minimized.

5. Application to Inspection Simulation

The ultrasonic signals picked up by a transducer in a - as an example - pulse-echo inspection experiment are determined in the following way. First, the transducer-generated displacement distribution is calculated at the position of the scatterer using Eq. (14), then the scattered wave field is determined as described in detail in (Spies, 2000). The (time-domain) signal detected by the transducer is finally determined using Auld's reciprocity theorem which exploits the displacement and traction at the

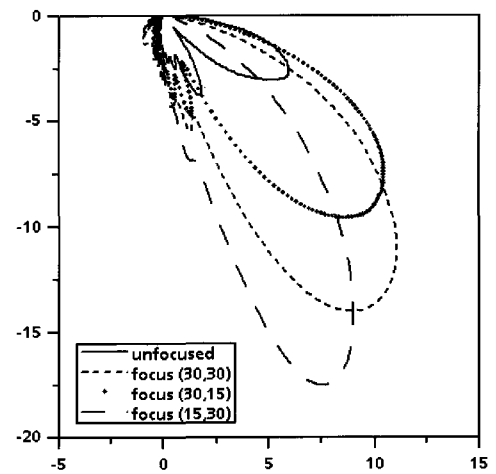

Fig. 4 Polar plots of the beam field directivity patterns calculated at a distance of $r = 40$ mm for various focal modes at indicated in the legend (composite's layers parallel to the surface).

scatterer's position in presence and absence of the scatterer, respectively (Auld, 1979).

The far-field expressions for planar vibrating sources according to Eqs. (19) to (21) can be used to perform approximate calculations. Thus, a simple expression can be formulated e.g. for the amplitude dynamic curves (ADC) measured in a pulse-echo inspection experiment. With $\underline{\mathbf{R}}_T$ and $\underline{\mathbf{R}}_S$ designating the spatial coordinates of the transducer and the planar scatterer, respectively, the magnitude of the particle displacement detected by the transducer can be expressed according to

$$|\underline{\mathbf{u}}_\alpha(\underline{\mathbf{R}}_T)| \cong U_0 \cdot \mathcal{R}(\widehat{\underline{\mathbf{R}}_T - \underline{\mathbf{R}}_S}) \cdot \frac{A_T A_S}{|\underline{\mathbf{R}}_S - \underline{\mathbf{R}}_T|^2} \cdot \Gamma_T^2(\underline{\mathbf{R}}_S - \underline{\mathbf{R}}_T) \cdot \Gamma_S(\underline{\mathbf{R}}_T - \underline{\mathbf{R}}_S). \quad (22)$$

$A_{T/S}$ and $\Gamma_{T/S}$ are the constant factors and the directivity functions characterizing the transducer and the scatterer, respectively, as specified in Eqs. (20) and (21). Additionally, the respective reflection coefficient $\mathcal{R}(\widehat{\underline{\mathbf{R}}_T - \underline{\mathbf{R}}_S})$ has been introduced to account for the reflection of the incident wave field at the defect. Although the influence of the traction-free material surface on the transducer radiation characteristics as well as the particular boundary conditions at the scatterer are neglected in using this relationship, the results compare well with those obtained on the basis of Eq. (14) (Spies, 2002a).

5.1. Calculation of Defect Scattered Signals

The addressed problem is to predict the signal from reflectors in a solid, observed in a pulse-echo measurement. It is assumed that normally incident longitudinal waves and obliquely incident transverse and longitudinal waves in an immersion geometry are used. A circular, unfocused transducer of 12.7 mm (half inch) diameter and of 5 MHz center frequency is considered. Three sets of scattering objects are considered: spherical pores, circular cracks and of cylindrical scatterers, centered at a distance of 25.4 mm into an aluminium block. They have respective diameters of 0.125 mm, 0.25 mm, 0.5 mm, 1 mm, 2 mm and 4mm. The smallest diameters are in the regime in which the defect is small with respect to the wavelength.

The signal observed during the normal incidence reflection from the front surface of the aluminum block is shown in Figure 5. The transducer to front-surface distance is taken to be 50.8 mm, which places the surface into the transducer nearfield. The beam fields have been calculated in water, as well as in the aluminum block assuming a water path of 50.8 mm. The normal incidence results have been shown in (Spies, 2002c), while the results for oblique transverse and longitudinal wave incidence, respectively, have been exemplarily shown for the 45°-case in (Spies, 2003a).

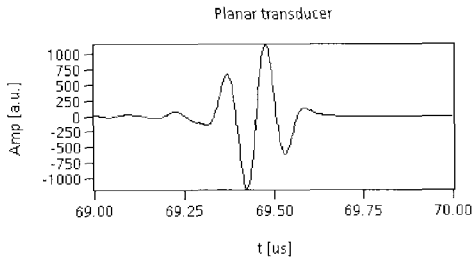

Fig. 5 Reference signal calculated for the circular, unfocused transducer of 5 MHz center frequency.

Figure 6 displays the maximum flaw signal amplitudes as a function of the reflector diameter for both normally and obliquely incident longitudinal waves. For each configuration, the signal amplitude for the 4 mm reflector is maximal and has accordingly been set to 0 dB. The results obtained for transverse waves and for the focused transducer in principle show the same behavior.

The results obtained for the circular cracks reveal that the amplitude is principally proportional to the square of the reflector radius, as far-field relationships also suggest (Spies, 2003a). This holds for both normal incidence and oblique incidence, where the circular crack has been assumed to be perpendicularly oriented with respect to the incident central ray. Thus, dividing the scatterer's diameter by a factor of 2 leads to a decrease of the scattered signal amplitude by a factor of 12 dB. However, referring to the larger scatterers (1, 2 and 4 mm diameter) the decrease in amplitude is less than 12 dB. This is due to the beam field amplitude variation across the defect surface (Spies, 2002c).

For the cylindrical and the spherical reflectors, in principle the expected amplitude behavior is also obtained. Here, additional calculations have been performed for a reflector diameter of 3 mm. Dividing the defect diameter by a factor of two leads to a decrease of the scattered signal amplitudes by a

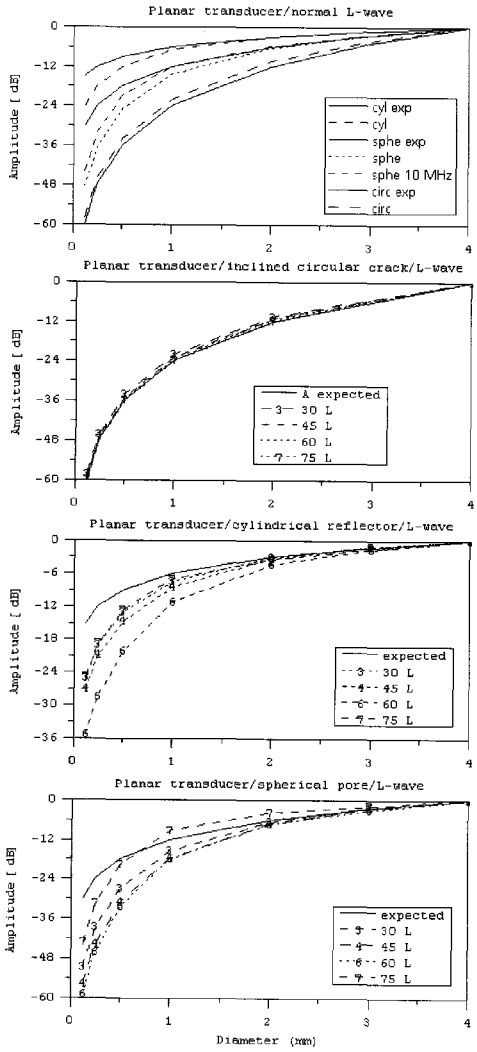

Fig. 6 Flaw signal amplitude plotted versus reflector diameter for normal (top) and oblique (bottom) L-wave incidence (unfocused transducer). The expected amplitude behavior according to Eqns. (3-5) is indicated by the solid lines. Similar diagrams result for the focused transducer as well as for incident transverse waves.

factor of 3 dB and 6 dB, respectively, for the 2, 3 and 4 mm reflectors, while for the smaller diameters, the decrease of the calculated amplitudes is larger. As the results obtained for the spherical pores for a frequency of 10 MHz reveal, the deviation from the expected behavior depends on the respective ratio of wavelength to reflector diameter. At 10 MHz, the deviations from the expected amplitude behavior occur at a reflector diameter of 1 mm, while in the 5

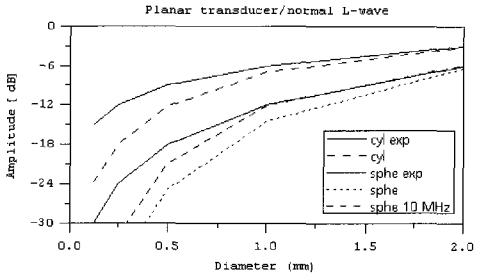

Fig. 7 Enlarged view of the signal amplitude plotted versus diameter for the cylindrical and the spherical reflectors (unfocused transducer, normal L-wave incidence at 5 and 10 MHz, respectively). The expected amplitude behavior according to Eqn. (4) and (5) is indicated by the solid lines.

MHz-case, the deviation of calculated from the expected amplitude drop already occurs at a diameter of 2 mm (Fig. 7).

The scattering process has been considered by using Kirchhoff's approximation, which assumes that each point on the scatterer's surface behaves like a point on an infinitely long reflecting plane. Although the $k \cdot r$ values (wavenumber times scatterer's radius) are small for some of the defects considered, the obtained results suggest that here Kirchhoff's approximation is still applicable for the case of planar scatterers, which is consistent with measurements recently performed on flat-bottomed holes using far field conditions (Schmitz and Spies, unpublished). However, from the results obtained for the cylindrical and the spherical reflectors it can be inferred, that the application of Kirchhoff's theory in the employed point source superposition technique leads to deviations from the expected amplitude behavior for curved scatterers in the regime where $k \cdot r$ is equal to 5 and less. The results obtained for the circular cracks and the spherical pores are consistent with those in (Gray and Thompson, 2001), where both approximate and exact models have been applied. In principle, the latter have shown that the amplitude decrease for the small scatterers is larger than predicted by Kirchhoff models.

5.2. Amplitude Dynamic Curves in Composites

Two unidirectionally carbon-fiber reinforced composite specimens with fibers being orientated at

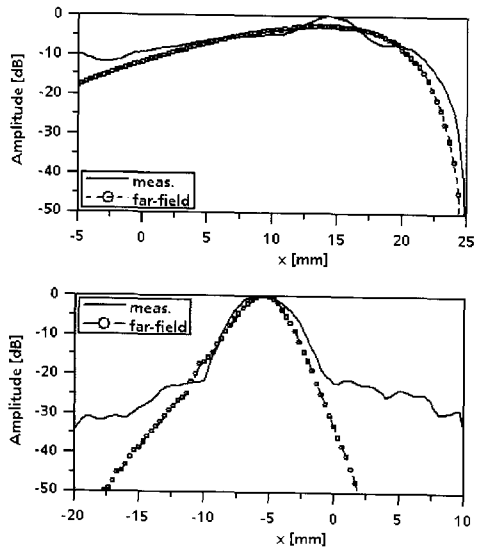

Fig. 8 Simulated and measured pulse-echo amplitude dynamic curves for 5 mm flat-bottomed holes in a unidirectional composite. The fibers are aligned at an angle of 15° (top, defect depth 15 mm) and 75° (bottom, defect depth 30 mm) to the surface. Note the different scan paths ($x = 0$ mm marks the lateral defect position).

15° (No. 1) and 75° (No. 2) to the surface, respectively, have been examined. These specimens were supplied with a number of 3 mm and 5 mm flat-bottom holes (FBH) at various depths. The pulse-echo experiments have been performed with a piezoelectric normal-transducer of 2.25 MHz frequency and 6.3 mm in diameter (Krautkrämer MSW-QC 2,25), generating (quasi-) longitudinal waves. Further details on the measurements can be found in (Spies and Jager, 2003b). For these inspection parameters, amplitude dynamic curves (ADC) have been simulated using the far-field relationships. As an example, Figure 8 shows the results obtained for 5 mm FBHs, which were located in a depth of 15 mm in specimen No. 1 and in a depth of 30 mm in specimen No. 2. In the latter case, the measured ADC does not drop below -30 dB, due to the experimental noise level. In these results, the effects of wave field spreading and skewing are more or less apparent. Good agreement between the simulated and the measured ADCs is obtained, with differences in the order of about 2 to 3 dB.

6. Summary

Analytical approaches to model ultrasonic nondestructive evaluation in general allow for reasonable calculation times. These models can be employed to consider the various wave phenomena separately, which is desirable from the practical point of view. Since approximations are applied, the approaches have to be selected according to the respective problem of interest. The presented methods are three-dimensional approaches and have been verified in comparison with experimental results previously. For frequencies in the range from 0.5 to 5 MHz, which is usually of interest in ultrasonic NDT, point source superposition provides simulation results within minutes on standard PCs, while calculations based on the far-field approximation can be performed within seconds. The presented simulation methods can be efficiently employed to clarify wave propagation effects and to optimize transducers as well as inspection procedures.

References

Auld, B. A. (1979) General electromechanical reciprocity relations applied to the calculation of elastic wave scattering coefficients, Wave Motion, Vol. 1, pp. 3-10

Gray, T. and Thompson, R.B. (2002) Solution of an Ultrasonic Benchmark Problem within the Paraxial Approximation, in D.O. Thompson and D.E. Chimenti (Eds.), *Review of Progress in QNDE*, AIP, Melville, New York, Vol. 21, pp. 1925-1932

Guo, Q.C. and Achenbach, J.D. (1995) Radiation of Ultrasound into an Anisotropic Solid, Ultrasonics, Vol. 33, pp. 449-456

Hosten, B., Deschamps, M. and Tittmann, B.R. (1987) Inhomogeneous wave generation and propagation in lossy anisotropic solids, J. Acoust. Soc. Am., Vol. 82, pp. 1763-1770

Pao, Y.H. and Varatharajulu, V. (1976) Huygens' Principle, Radiation Conditions and Integral Formulas for the Scattering of Elastic Waves, J. Acoust. Soc. Am., Vol. 59, pp. 1361-1371

Schmitz, V. and Spies, M. (unpublished) Measurements on an Aluminum Block with Flat-Bottomed Holes Using Pulse-Echo Contact Technique

Spies, M. (1994a) Transducer-modeling in general transversely isotropic media via point-source-synthesis. Theory, J. Nondestr. Eval., Vol. 13, pp. 85-99

Spies, M. (1994b) Elastic waves in homogeneous and layered transversely isotropic media: plane waves and Gaussian wave packets. A general approach, J. Acoust. Soc. Am., Vol. 95, pp. 1748-1760

Spies, M. (2000) Kirchhoff evaluation of scattered elastic wavefields in anisotropic media, J. Acoust. Soc. Am., vol. 107, pp. 2755-2759

Spies, M. (2001) Semi-analytical elastic wave-field modeling applied to arbitrarily oriented orthotropic media, J. Acoust. Soc. Am., Vol. 110, pp. 68-79

Spies, M. (2002a) Quantitative evaluation of defects in anisotropic media using the far-field radiation characteristics of vibrating sources, in D.O. Thompson and D.E. Chimenti (Eds.), *Review of Progress in QNDE*, Plenum Press, New York, Vol. 21, pp. 107-114

Spies, M. (2002b) Modeling Transient Radiation of Ultrasonic Transducers in Anisotropic Materials Including Wave Attenuation, in D.O. Thompson and D.E. Chimenti (Eds.), *Review of Progress in QNDE*, AIP, Melville, New York, Vol. 21, pp. 807-814

Spies, M. (2002c) Simulating a Standard Type Problem of Ultrasonic Testing - A Contribution to the Comparison of Models, in D.O. Thompson and D.E. Chimenti (Eds.), *Review of Progress in QNDE*, AIP, Melville, New York, Vol. 21, pp. 1949-1955

Spies, M., Gebhardt, W. and Rieder H. (2002) Boosting the Application of Ultrasonic Arrays, in D.O. Thompson and D.E. Chimenti (Eds.), *Review of Progress in QNDE*, AIP, Melville, New York, Vol. 21, pp. 847-854

Spies, M. (2003a) Prediction of Transient Flaw Signals of the Ultrasonic Benchmark Problem, in D.O. Thompson and D.E. Chimenti (Eds.), *Review of Progress in QNDE*, AIP, Melville, New York, Vol. 22, pp. 1792-1799

Spies, M. and Jager, W. (2003b) Synthetic aperture focusing for defect reconstruction in anisotropic media, Ultrasonics, Vol. 41, pp. 125-131

Spies, M. (submitted) Efficient Optimization of Single and Multiple Element Transducers for the Inspection of Complex-Shaped Components, NDT&E International, submitted for publication

Wu, K., Nagy, P.B. and Adler, L. (1991) Far-field radiation of a vibrating point source in anisotropic media, J. Nondestr. Eval., Vol. 10, pp. 71-78

Wu, K., Nagy, P.B. and Adler, L. (1990) Far Field Radiation of a Point Source on the Free Surface of Semi-Infinite Anisotropic Solids, in D.O. Thompson and D.E. Chimenti (Eds.), *Review of Progress in QNDE*, Plenum Press, New York, Vol. 9, pp. 149-156

Stenzel, U. and Brosze, O. (1958) *A Guide to the Calculation of Sound Processes*, Springer, Berlin, in German